



X-ray CT analysis of the evolution of ballast grain morphology along a Micro-Deval test: key role of the asperity scale

Ivan Deiros Quintanilla^{1,2} · Gaël Combe^{1,2} · Fabrice Emeriault^{1,2} · Charles Voivret³ · Jean-François Ferrellec³

Received: 21 November 2018
© Springer-Verlag GmbH Germany, part of Springer Nature 2019

Abstract

Ballast grains in railway tracks progressively wear due to the efforts exerted by the continuous passage of trains and the periodic maintenance operations. The initial sharp edges and vertices of the grains tend to become smoother and the surface texture is removed. This change in morphology plays a key role on the proper behaviour of the ballast layer and, consequently, on the frequency maintenance required on the track. The object of this paper is to improve the understanding of the wear process by tracking the morphology of a sample of grains submitted to an accelerated ageing using the Micro-Deval standard test. To this goal, X-ray Computed Tomography is used to scan a sample of grains at different states of wear and the resulting images are compared using 3D image analysis. A description of morphology evolution at different scales is provided using scalar parameters and spherical harmonic analysis, proving that the general form is not significantly changed during a standard Micro-Deval test. Thus a detailed analysis at the asperity level is performed, showing the key role of the edge broadening and vertex smoothing phenomena on ballast wear.

Keywords Railway ballast · X-ray CT · Grain morphology · Micro-Deval

1 Introduction

Ballast, as the layer of coarse grains located immediately below the sleepers, plays a key role in the degradation of the railway track. After some years of high-speed railway lines (HSL) in France, ballast grains proved not to be resistant enough, suffering a fast degradation.

Ballast layer is formed by centimetric-sized, ranging from 25 to 50 mm, sharp aggregates with a very homogeneous grain size distribution. The mineralogy of the grains will usually depend on the available materials in the country and in the closer quarries. However, due to its high performance and availability, granite is the first option for most French railway lines, especially for HSL. Hence, ideal ballast has

an homogeneous size and it is clean from fine particles, it presents a high angularity and a high resistance to wear. However, even with the strictest selection methods, under the combination of both the dynamic stress imposed by traffic and maintenance operations, ballast is gradually worn by fragmentation of grains and attrition at the contacts. The direct consequence of this degradation is the evolution of grain size and form: the grading curve is shifted toward smaller particles, steadily producing fine particles in the process, and grain form tends toward more rounded grains that progressively lose the characteristic sharpness and angularity of new ballast.

The loss of angularity reduces the interlocking forces and the anisotropy of the contact network, which results in a gradual decrease of the shear strength of the layer [4]. This decrease in the track performance consequently reduces the time before track defaults reappear, leading to progressively shorter maintenance cycles. Eventually, ballast layer needs to be substituted in what represents a costly operation for the railway industry, thus this is a well-known problem of all countries that have traditionally invested in ballasted tracks and many efforts have been put into extending ballast lifespan.

✉ Ivan Deiros Quintanilla
ivan.deirosq@gmail.com

Gaël Combe
gael.combe@3sr-grenoble.fr

¹ Université Grenoble Alpes, 3SR, F-38000 Grenoble, France

² CNRS, 3SR, F-38000 Grenoble, France

³ SNCF Réseau, Direction Ingénierie et Projets,
93574 La Plaine Saint-Denis, France

Several works have been focused on identifying the sources and influence of fine particles and particle breakage on the behaviour of the ballast layer [18, 25, 38]. Other have tried to correlate the resistance indexes of the aggregates resulting from standard tests performed in the quarry, such as Micro-Deval and Los Angeles, with the lifespan of ballast [24, 30].

On the other hand, the influence of particle form on the mechanical behaviour of granular media, included ballast, has been much studied [3, 27, 36]. Grain angularity has been proven to improve significantly the shear resistance of the layer, and discrete element simulations have been improved in consequence to take into account this phenomenon. Particle form modelling has evolved from simple spheres to clusters of spheres [10, 19, 26, 29, 41] or polyhedra [2, 35, 37, 39, 40]. And the continuous increase of computer capacity and the optimization of modelling techniques opens the door to the usage of realistic particles, detailed up to the point of generating the desired angularity to model the state of wear of the grains [34].

The evolution of grain form is thus required to assess the rate grains lose their angularity. In long-term systems such as river flows, this process was studied by Domokos et al. [9], identifying two separate phases, involving a decrease of angularity before a significant modification of the general form.

In this paper a detailed analysis of the morphology evolution during the first phases of wear is presented, focusing on the loss of surface roughness and angularity for the particular case of granite ballast grains. To that purpose, a sample of grains are subjected to an accelerated ageing using the Micro-Deval standard attrition test. An image analysis using X-ray Computed Tomography is then performed at different states of wear.

2 Experimental campaign

2.1 Test procedure and tools

2.1.1 Micro-Deval

Attrition resistance of ballast aggregates is experimentally assessed in a Micro-Deval device, following the corresponding European railway standards [32, 33]. In this test, a sample of 10 kg of ballast (≈ 100 grains) is left turning for 140 min at 100 rpm inside a steel hollow cylinder 400 mm long and with an inner diameter of 200 mm. The numerous contacts within the device, both between grains and with the steel drum, produce an accelerated wear in the aggregates, producing fine particles and causing changes in their morphology.

This test is hence convenient to produce an accelerated ageing in the grains. Besides, the device allows for stopping the rotation as desired, making it possible to track the evolution of the sample along the test. For this purpose, a sample of 10 kg of granite aggregates, fulfilling the standard requirements for HSL ballast in terms of resistance and grain-size distribution, was selected and tested in the Micro-Deval. The test was performed in dry conditions (i.e. no addition of water in the cylinder). From the sample, seven different ballast grains were identified and marked as shown in Fig. 1. These seven grains were arbitrarily chosen searching for heterogeneity in terms of forms and colours, although slightly above the average concerning size. They were then scanned at different states of wear in order to track their morphology changes.

Previous works on the Micro-Deval test [8] showed that the wear rate along the test is progressively decreased, tending to a constant production of fine particles, i.e. during the first half of the test grains lose a significant higher amount of mass compared to the second half. Consequently and in order to better track this phenomenon, during this morphology analysis, scans were not programmed at regular intervals, but instead at 0, 10, 30, 70 and 140 min of cumulated Micro-Deval time.

2.1.2 X-ray computed tomography

At the beginning of the experimental campaign (new grains) and at each of the programmed stops, all seven grains are removed from the 10 kg sample, scanned using X-ray CT and reintroduced to the sample for the next Micro-Deval cycle. X-ray CT was used due to the availability of the device in the laboratory, although other methods such as 3D scans are often used for ballast scanning [34].

During a CT slice, an X-ray source emits rays towards the specimen having a detector screen on the opposite side. The density of the material through which the X-rays have to pass will determine the grey scale on the output image [1, 16]. Taking several slices at different angles, it is possible to reconstruct a 3D image of the specimen. The resolution chosen for this project is 50 $\mu\text{m}/\text{voxel}$, which is high enough



Fig. 1 Sample of seven ballast grains used for the morphology analysis. For identification purposes, grains were named as SX, being X the number noted on the grain surface

to describe all the features of the surface of ballast grains and low enough to be able to scan up to seven grains in a single day. The reconstruction of each grain is then performed using 1440 projections per full tomography, obtaining an STL mesh file, output that is later processed using Python and MeshLab.

2.2 Qualitative comparison

Along the Micro-Deval test, grains change form as they wear: surfaces become smoother losing their initial roughness and sharp angles are progressively rounded. These features can be observed in Fig. 2, which shows the scan of the grain S6 new and after 140 min of Micro-Deval. Although the grain is still recognizable and the general form is conserved, the initial sharpness of edges and vertices has been significantly reduced and some tips have been removed from the grain.

Two different mechanisms of wear are observed when analysing the intermediate scans. The first one is a slow but constant degradation affecting faces, edges and vertices all along the test, continuously removing layers of matter and consequently smoothing the different surfaces and angles. The second one correspond to occasional local breakages of weak parts of the grain, affecting mainly to grain vertices due to their reduced cross-section, which remove larger chunks of matter and change the form of the grain. These local breakages do not always happen and when they do so, they usually affect small parts of the grain. Big breakages that split a grain in two parts of similar size are possible but rare. As a reference, from the seven grains of study, S6 shown in Fig. 2 was the one suffering the largest amount of local breakages along the test.

2.3 Evolution of the mass of the grains

Grains were weighted at each wear state in order to track the evolution of their mass and to identify the variability among

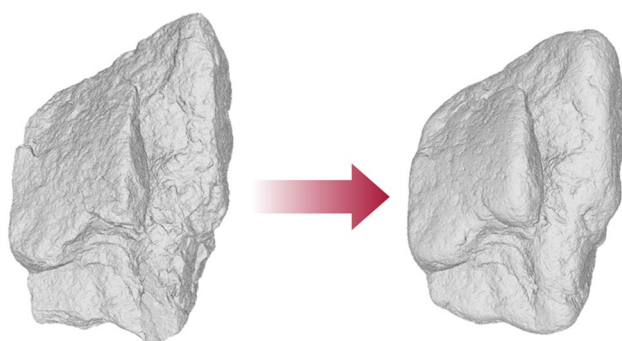


Fig. 2 State of specimen S6 before (left) and after (right) of a standard Micro-Deval test (140 min)

the sample. In addition, the mass of the full 10 kg sample was also tracked for comparison. Incidentally, darker grains were found to be slightly denser ($\sim 3\%$) than lighter ones.

Figure 3 shows the decrease in percentage of the mass of each individual grain and of the whole sample of 10 kg. It can be noticed that all grains have a higher loss rate at the beginning of the test and it tends to a constant rate by the end. This is the same trend already observed in the previous Micro-Deval tests [8]. Furthermore, except S6, which suffered some relatively big breakages all along the test, all other specimens show approximately a mass loss of between 2% and 3% by the end of the test, which is of the same order of magnitude as the full sample. The particular form of each grain does not seem to affect significantly the final amount of wear. The larger the size of the grains, the higher the probability of eventual weaker parts, which could explain why all of them are slightly above the average wear of the sample, but the difference is neither significant nor concluding.

3 Evolution of grain descriptors

In order to describe the morphology of a particle, there is a large number of quantities, parameters and definitions used in the literature. Implicitly or explicitly, most of these parameters characterizing the morphology are classified or ordered using different levels or scales, depending on how general or how in detail the parameter describes the grain. Some authors [31] divide this classification into three different levels: form (macro-scale), angularity (meso-scale) and texture (micro-scale). This transition in scale is considered in the following sections.

3.1 Form parameters (Zingg's diagram)

The typical way of describing the general form of a grain is by defining its three characteristic lengths, which are

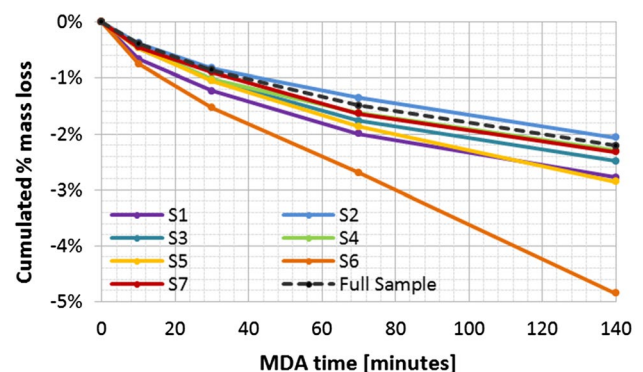


Fig. 3 Cumulated mass percentage lost along the Micro-Deval test by each of the seven grains and by the whole package of grains

given by inscribing the grain into a rectangular prism (Fig. 4). The lengths correspond then to the sides of that cuboid: S (shortest), I (intermediate) and L (longest). There are multiple ways of choosing the definition of the circumscribing prism, which give slightly different results. The method applied in this project defines the three sides of the prism following the three principal directions of inertia of the grain. As it will be observed, this choice is not determinant on the conclusions extracted.

From these three characteristic lengths, several parameters describing the form can be defined [5, 22], all of them presenting approximately the same trends. As an example, in this paper the evolution of the Elongation Ratio (ER) and Flatness Ratio (FR) will be shown:

$$ER = I/L \quad (1)$$

$$FR = S/I \quad (2)$$

According to the presented definitions, both parameters range from 0 to 1, the latter value corresponding to the case of either a sphere or a cube. Table 1 shows the initial values

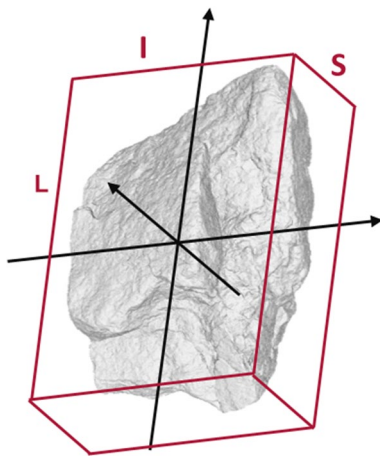


Fig. 4 Characteristic lengths of a particle: L (long), I (intermediate) and S (short). They are defined using a circumscribed rectangular prism oriented following the principal directions of inertia of the grain

of the mass, the three characteristic lengths and the form parameters ER and FR for all seven specimens.

ER and FR are commonly represented together in Zingg's diagram [43]. Zingg proposed a basic classification of four different grain forms (blades, rods, disks and spheroids), by establishing an arbitrary threshold at 2/3 for both parameters as it can be seen in Fig. 5.

Figure 5 shows the evolution within Zingg's diagram of the seven grains along the Micro-Deval test. It can be observed that grains present almost no evolution of the form. Only S1 and S6 present a slight change in form due to the local breakages suffered. However, not even these two grains present a change in Zingg's category, and they do not show neither a trend towards the form of a sphere (upper-right corner).

In conclusion, a standard Micro-Deval test (140 min), despite clearly wearing the grains, has proven not to be aggressive enough to produce significant changes on the general form of the grains. The imperceptible change on the general form

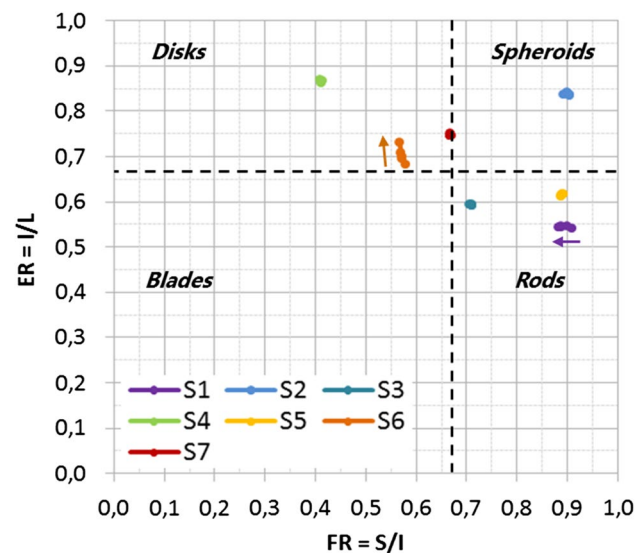


Fig. 5 Zingg's diagram: representation of the evolution of the parameters ER and FR along the Micro-Deval test. As a reference, the upper-right corner of the plot corresponds to the form of a sphere or a cube

Table 1 Initial characteristics and form parameters of all seven specimens

	Mass (g)	L (mm)	I (mm)	S (mm)	ER	FR
S1	146.13	86.98	47.10	42.84	0.542	0.910
S2	142.64	63.80	53.31	47.61	0.836	0.893
S3	126.55	78.86	46.90	33.38	0.595	0.712
S4	155.70	79.92	69.56	28.49	0.870	0.410
S5	179.95	82.69	50.58	44.93	0.612	0.888
S6	148.08	83.75	57.20	33.19	0.683	0.580
S7	103.71	64.63	48.49	32.34	0.750	0.667

while the angularity is reduced during a first phase of wear was identified by Domokos et al. [9] for pebbles in rivers.

3.2 Spherical harmonics analysis

3.2.1 Definition and assumptions

When a multi-scale description of the morphology is needed, other methods that can deal with all three levels of description are commonly used. Fourier analysis of the contour can be used when dealing with 2D particles [42], obtaining different signatures for different scales depending on the frequencies. If a 3D description is needed two methods are used to analyse image data: wavelet method [20] and spherical harmonic analysis (SHS) [11]. The second method has been chosen for this project, since it was originally used to deal with 3D X-ray CT data.

The data given by an imaging device such as X-ray tomography can be expressed as a discrete cloud of points. It is then possible to express the coordinates of all points forming the contour surface of the grain using spherical coordinates on the form $R(\theta, \phi)$, where R is the radial distance from the centre of mass of the particle to each surface point, $\theta \in [0, \pi]$ is the polar coordinate and $\phi \in [0, 2\pi)$. The idea of this method is to describe the morphology of the grain using spherical harmonic series, where as we consider more and more coefficients (longer series), the detail of the description becomes higher. By establishing thresholds, it is possible to describe all three scales of morphology: form, angularity and texture.

The spherical harmonic series are expressed as:

$$R(\theta, \phi) = \sum_{n=0}^{\infty} \sum_{m=-n}^n a_{nm} \cdot Y_n^m(\theta, \phi) \quad (3)$$

where Y_n^m are the spherical harmonic functions:

$$Y_n^m(\theta, \phi) = \sqrt{\frac{(2n+1) \cdot (n-m)!}{4\pi \cdot (n+m)!}} \cdot P_n^m(\cos(\theta)) \cdot e^{im\phi} \quad (4)$$

where P_n^m are the associated Legendre polynomials. The system can then be solved using a matrix notation of the form $R_{(N \times L)} = Y_{(N \times L)} \times a_{(L \times 1)}$ [23], where $L = (n_{max} + 1)^2$ and N the number of voxels of the surface. The description of form, angularity and surface texture is then based on the signatures given by the coefficients a_{nm} , by using the thresholds proposed by Masad et al. [28]:

$$Form = \sum_{n=1}^4 \sum_{m=-n}^n |a_{nm}| \quad (5)$$

$$Angularity = \sum_{n=5}^{25} \sum_{m=-n}^n |a_{nm}| \quad (6)$$

$$Texture = \sum_{n=26}^{n_{max}} \sum_{m=-n}^n |a_{nm}| \quad (7)$$

As a reference, for a perfect sphere all three signatures would be equal to 0.

Due to their intrinsic definition, the development of these series quickly requires a large amount of computational memory and time. Therefore some restrictions had to be introduced, searching for a compromise between the computational time and the precision on the result. For this reason, following the work of Masad, a limit of $n_{max} = 30$ was considered. This way, it is possible to define form and angularity following the thresholds set at $n = 4$ and $n = 25$, and there are still five coefficients remaining to give information about texture.

In addition, a simplification of the original meshes was required to reduce the number of elements from ~ 5 million to 250,000 elements. The reduction of elements was made by decimation using an internal algorithm of MeshLab called Quadratic Edge Collapse Decimation [12, 15], which resulted in a very acceptable simplification preserving all the topological features. A convergence analysis was performed on all three SHS morphology signatures by comparing meshes from 5000 to 500,000 elements. It was observed that, after 100,000 elements, the error on the measurements was stabilized below 0.1%. However, since the computational cost was still acceptable, meshes of 250,000 elements were used. These reduced meshes were also used on the asperity analysis in Sect. 4.

3.2.2 Evolution of SHS signatures

Figure 6 shows the evolution in percentage of all three SHS signatures along the Micro-Deval test for each individual grain. It can be observed that all three parameters decrease all along the test tending to a more rounded particle. The decrease follows the same trend as the mass, it is more prominent during the first minutes of test tending to reach a stable decreasing rate by the end of the test. However, whereas the general form presents a relatively small evolution ($< 2\%$), confirming the conclusion of the previous Sect. 3.1, angularity and texture present a cumulated decrease of more than 10% by the end of the test.

Angularity is affected by those asperities lying on the edges and vertices, it shapes the external profile of the grain and thus slightly influences the general form of the grain and also its micro-morphology. On the other hand, texture is mainly given by asperities lying on the faces of the particle, not affecting the general form of the grain but only the micro-morphology. However, from a micro-scale point of view, both parameters are strongly related to the asperities of the particle, only differing on the location of those asperities.

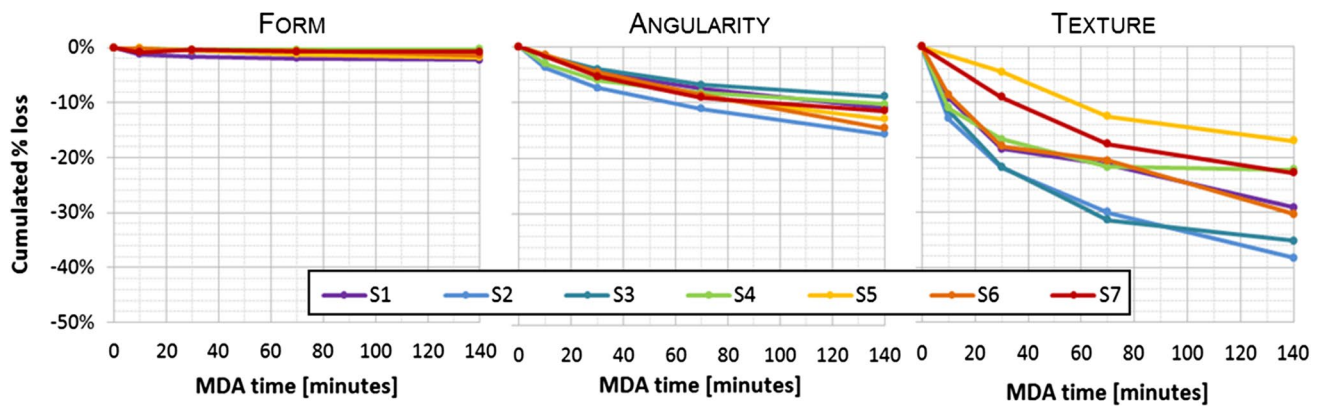


Fig. 6 Evolution for all seven grains of the three signatures of the SHS analysis corresponding to the three scales of morphology: general form, angularity and surface texture

In conclusion, except for eventual major breakages, most of wear comes from smoothing edges and vertexes and removing the surface texture, reaffirming the visual inspection of grain wear presented in Sect. 2.2. Convex features are the most exposed to external contacts so, in a system with a random distribution of impacts and contacts such as within the Micro-Deval cylinder, these convex asperities tend to suffer a higher number of them. In addition, small tips and sharp edges present smaller cross sections by definition, which renders them weaker and eventually unable to resist aggressive wear. To obtain direct confirmation of these hypotheses, a detailed analysis at the asperity scale is presented in the following section.

4 Analysis at the asperity scale

4.1 Definition of curvature and asperity radius

In order to study the morphology at the asperity scale, the evolution of local curvature (or its reciprocal, the radius of the asperity) has been analysed. For planar 2D curves, curvature at any point P can be defined as the rate of change of the tangent line, which is equivalent to the reciprocal of the radius of the best-fitting osculating circle at that point P [13, 21]:

$$\kappa = \frac{1}{R} \quad (8)$$

where R is the radius of the circle (Fig. 7). For surfaces, curvature is more complicated to define due to the fact that it needs to capture the rate of change of the surface from the tangent plane, but the concept of a best-fitting sphere, which radius is the reciprocal of the curvature, can still be applied to compute the mean curvature. This approach is used by the

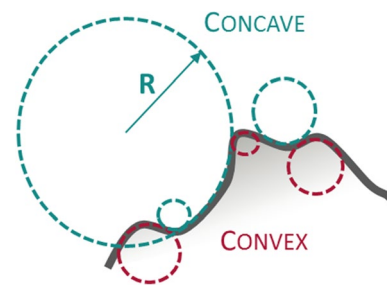


Fig. 7 Definition of curvature as the inverse of the radius of the best-fitting circle at each point of the curve. This concept can be extrapolated for the 3D case using spheres. The neighbour points are taken into account for the fitting in a larger or lower scale depending on a filter scale parameter

algorithm called Algebraic Point Set Surfaces [14] included in MeshLab package.

This algorithm shows robustness and a good fit to the actual morphological features of the grain. Furthermore, it includes a filter scale parameter, which determines the radius of surrounding area that will be considered when computing the best-fitting the sphere, i.e. how locally the curvature will be computed. Figure 8 shows the result of applying the algorithm at different filter scales.

A smaller scale gives information about finer details but loses information about the local convexity of the surrounding area. For this project, an arbitrary choice of filter scale = 10 was made, searching for a compromise between detail but also considering the area usually involved on ballast-ballast contacts. This value of filter scale allows for studying asperities presenting a radius larger than 0.3 mm. This is an arbitrary choice based only on qualitative data, an optimal answer does not exist. However, results extracted when using the previous and next scale values (8 and 12) do not differ significantly with respect to 10, leading to the same conclusions. Concerning finer asperities ($R < 0.3$ mm) which could

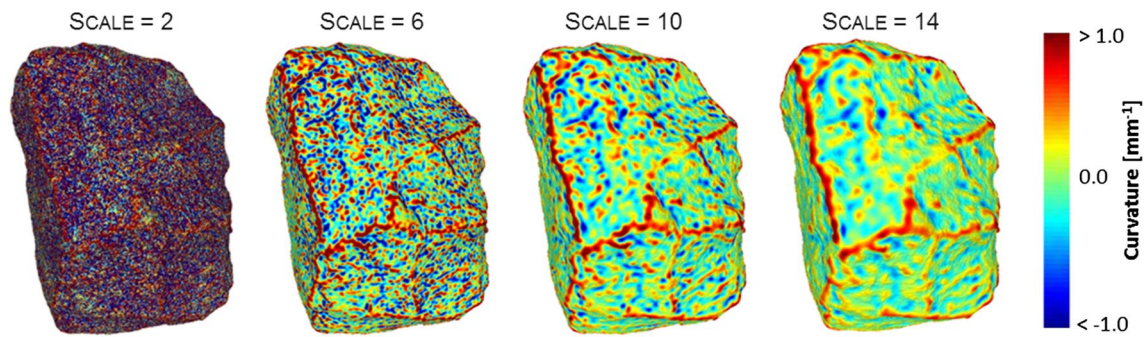


Fig. 8 Computation of curvature over the surface of S7 considering different filter scales. Negative curvature corresponds to concave asperities and positive to convex ones. An arbitrary choice of Scale

= 10 was made, searching for a compromise between a good asperity detail and the inclusion of the neighbour area around the asperity

have a role on the contact behaviour, it will be shown in the following sections that small asperities ($R < 1$ mm) tend to quickly disappear from the specimens. There is no reason to think that this behaviour is not also extended to smaller asperities. The smoothing of these small asperities is, in any case, taken indirectly into account when computing the average local curvature of the grain.

Finally, for a more intuitive understanding of the results, the asperity radius was considered for the analysis instead of the curvature, computing first the curvature using the algorithm described above and then obtaining the radius of the asperity as the reciprocal of the curvature. The sign convention used considers concave asperities as negative curvature or radius, and hence convex features as positive.

4.2 Evolution of asperity radii

One way to observe the evolution of the asperity radii throughout the test is to compare the radii histograms before and after erosion. Figure 9 shows the difference between the normalized histograms before the test (0 min) and after a standard Micro-Deval test (140 min), negative values representing a decrease in the number of asperities in that range of radii. As it can be observed, all grains behave in a similar way regardless of their form. This similar distribution and evolution of asperities, allows for treating all the asperities of all the grains as if they belonged to a single grain without making distinctions. This will be applied in the following plots and analyses for better visualization and of the results.

Concave asperities tend to always decrease in number as the grains are worn. A possible explanation could be that, in an overall convex shape like that of an aggregate, in order to have a concave feature, it must be necessarily surrounded (closer or further) by convex features. Therefore, when the neighbour area is eroded, concavity is automatically decreased. In particular, very concave areas are especially sensitive to changes in the surroundings due to their small radius.

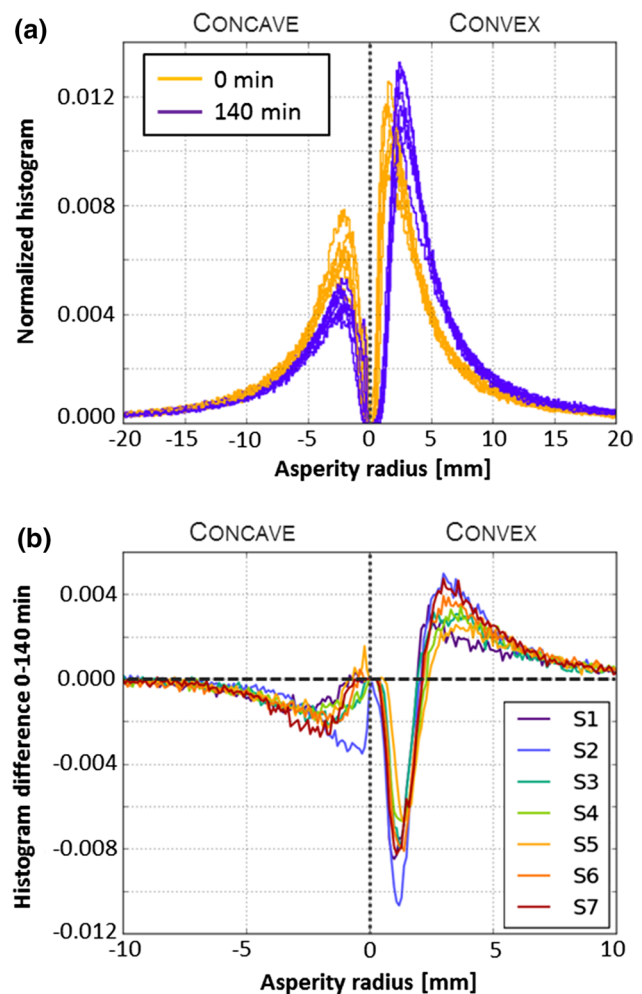


Fig. 9 **a** Normalized histograms of the asperity radii of the seven specimens for 0 min and 140 min of Micro-Deval test. **b** Difference of the histograms in (a) for each individual grain. Negative values indicate a decrease in number of asperities of that specific radius, and vice versa

The number of convex features, however, present different trends depending on their radius before erosion. These features are the most exposed to external contacts and impacts. Sharp tips and edges are also weak points of the grain, facilitating eventual breakages. Thus, these features are likely to quickly disappear from the grains. The direct consequence is that these surface points are automatically transferred to a higher radius category.

In Fig. 9, a threshold at an asperity radius of approximately 2 mm can be detected for all the grains, below which the number of asperities tend to decrease and vice versa. It is important to remark that this is a population balance problem: evidently features with larger radii than 2 mm also wear and evolve towards even larger radii, but the rate these features disappear is lower than the creation rate resulting from the evolution of smaller asperities.

However, the trends observed so far are extracted from the overall distribution of asperities and, although unlikely, it could be the consequence of a random process tending to a generally more convex shape of the grain, but not a direct evolution of individual features. In order to confirm the hypotheses, a monitoring of the evolution of the radius of each surface point is required. To do so, a K-D Tree algorithm was used [6], which consists on a space-positioning data structure for organizing points in a space of dimension K. It allows for associating each point within the original mesh with its best-fitting point within a second mesh.

Figure 10 shows a 3D normalized histogram (density represented by the colour) where, in the X-axis, the original asperity radii (i.e. grain before erosion) is plotted, and, in the Y-axis, it is plotted the increment in radius that those asperities suffered during the first 10 min of test. For convex asperities, an increase of the radius means a smoothing process, whereas a decrease means a sharpening process. For concave asperities, since their radius is originally negative, it is the opposite. The diagonal line $y = x$ represents, therefore, the surface points that doubled their radius.

The core of the density plot, formed basically by convex features of radius from 0.5 to 1.5 mm, is entirely located on the smoothing zone. These asperities consistently suffered an increase in radius but they rarely doubled their initial radius. This plot is almost identically reproduced on the successive cycles of erosion. The only difference, represented with the arrow in the figure, is that the density core and its associated dispersion cone are progressively shifted to the right. This is a consequence of sharpest asperities disappearing from the grain, resulting in new asperities (most likely with a larger radius) becoming the sharpest ones. The process is then repeated but shifted to slightly higher radius.

Figure 11 shows the location and evolution of convex and sharp asperities, i.e. $0 < R < 3$ mm, on specimen S3 during all five states of wear. As expected, these convex asperities are mainly located along the edges and on the vertexes.

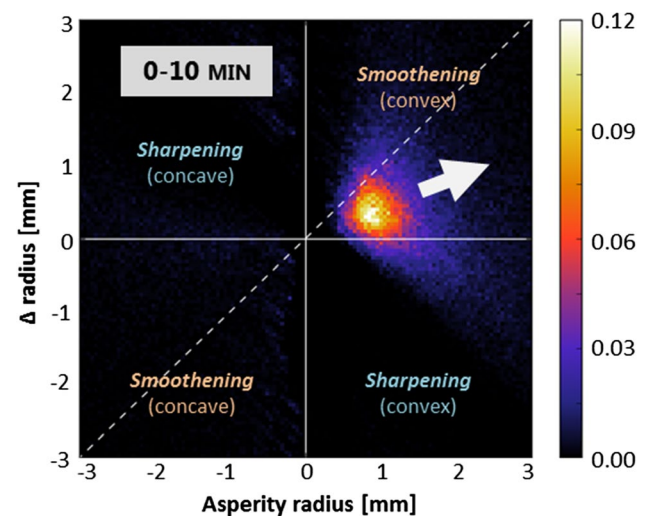


Fig. 10 Normalized 3D histogram (density represented by the colour) of the evolution of asperity radii during the first 10 min of Micro-Deval test. As the test proceeds, the trend remains similar but progressively shifting towards the right (larger radii), due to small asperities being smoothed or removed (colour figure online)

When the grain is new, the edge is narrow and sharp, with radius below 1.5 mm all along the line. During the first 10 min, these edges and vertexes wear, quickly evolving either by being removed or smoothed, while the points surrounding them remain relatively protected from contacts. As edges and vertexes are smoothed, neighbour points become more exposed and erosion starts happening over a larger area. Consequently, the edge enlarges presenting for every cycle a wider band of convex points. The overall radius is also increased and asperities ranging between 1.5 and 2.5 mm of radius become progressively more common on the edge.

4.3 Role of asperity radius on the wear process

In order to visualize and quantify the wear over the surface of the grains, the scans were pre-orientated using their principal directions of inertia and aligned using the built-in function of MeshLab by Iterative Closest Point [7]. Meshes are then compared in pairs in order to extract the difference using Hausdorff Distance [17], which provides a quality map over the surface of one of the two meshes. Henceforth, wear will be described as the distance between scans, and not in volume or mass.

Figure 12 shows the erosion of specimen S3 during all four erosion cycles. As expected, wear is happening mostly on edges and vertexes, whereas faces remain almost intact. At the beginning of the test, erosion is deeper and focused on the very edge of the grain, i.e. the area of influence is narrow but the maximal wear is higher. Sharp edges and tips get aggressive erosion due to their high exposition to

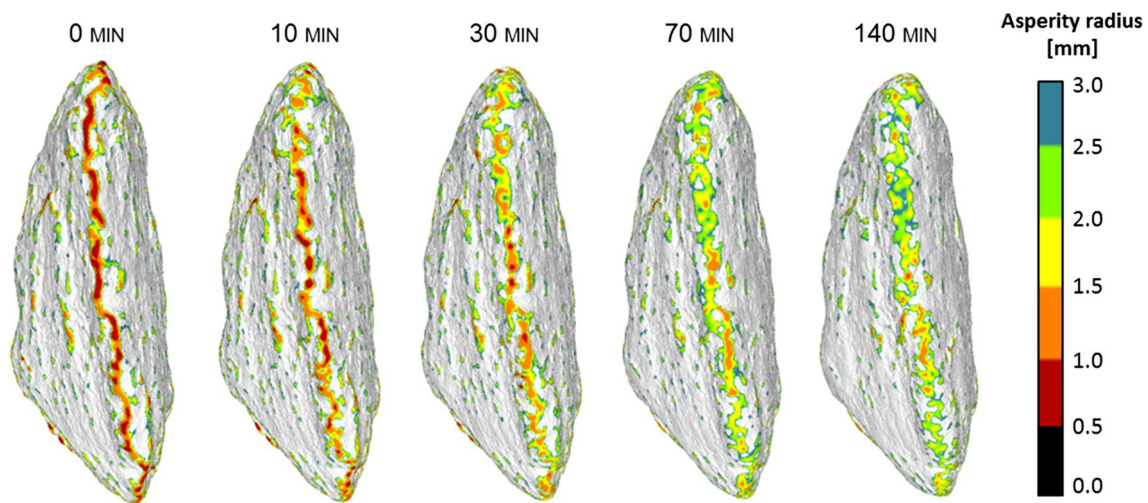


Fig. 11 Evolution of the radii of convex asperities of specimen S3. Sharp asperities, i.e. small radius, are mainly located on edges and vertices. These asperities are progressively smoothed reducing their

radius and enlarging their area of influence, broadening the edges and exposing new surface points to potential contacts

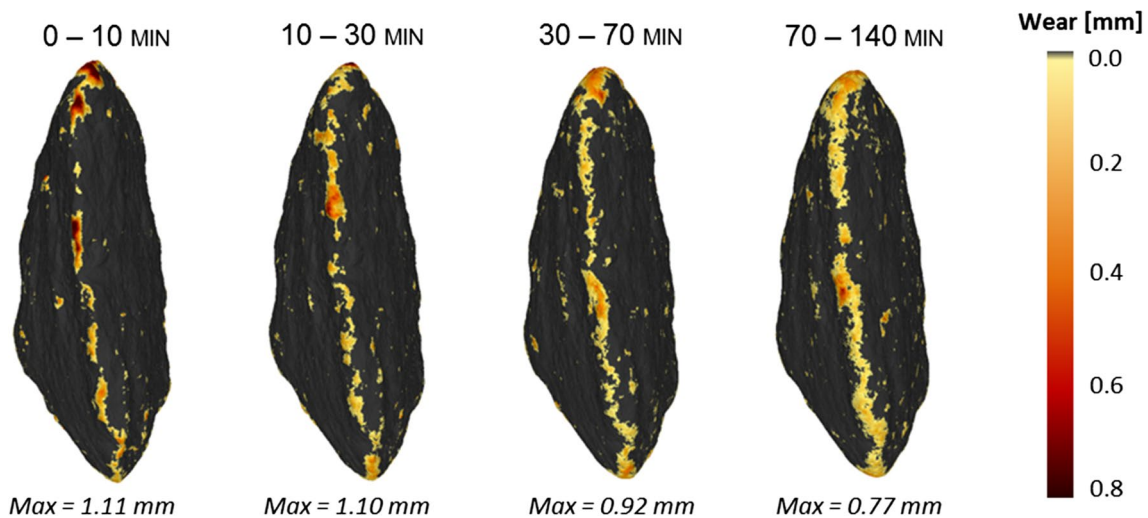


Fig. 12 Wear on specimen S3. Asperities suffering wear are coloured from light yellow to dark red, no wear is represented in black. Wear is mainly produced on edges and vertices, where sharp asperities are located. It shows a strong correlation with Fig. 11 (colour figure online)

contacts and intrinsic weakness, due to their associated small contact area and reduced cross section. As the test goes on, the area of influence of wear gets progressively wider, but the maximal local wear decreases, even though each cycle is longer than the previous one. As long as the weak parts are removed, edges and vertexes present a larger radius and thus a larger contact area and cross section, becoming more resistant to impacts and reducing the local wear rate. This behaviour is consistent with the results shown in the previous section and specifically in Fig. 11.

The smoothing of roughness (i.e. surface texture) on the faces is a more subtle phenomenon. It is mostly produced due to the destruction of isolated sharp asperities,

which produce a reduction on the roughness measurements. However, there is also a very fine smoothing process of the overall surface that is combined with the inclusion of some fines between the micro-asperities. This layer of fines can occasionally become so stuck to the grain that it is not removed by washing the grain with water. All in all, it leads to more even surface that can be felt just by touching the grain. Hence faces do not contribute significantly to the total production of fines, but there is indeed some wear happening on them.

This behaviour is confirmed by Fig. 13, which shows the normalized histogram of the asperities suffering at least 0.5 mm of wear. It can be observed that, within the range of a

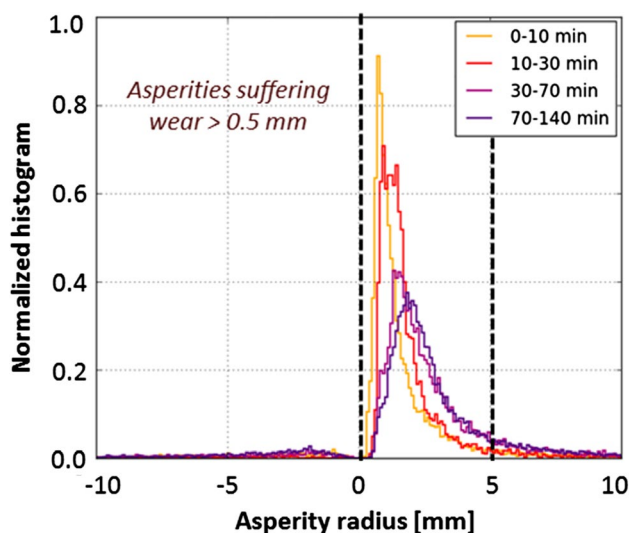


Fig. 13 Normalized histogram by asperity radius of asperities wearing more than 0.5 mm for each of the Micro-Deval intervals

standard Micro-Deval test, aggressive wear is almost exclusive of convex asperities with a radius below 5 mm.

There are however, some changes as the test evolves. During the first 10 min, wear mainly happens in asperities below 2 mm of radius. Asperities with a radius close to 0.5 mm generally present a very high absolute wear, even higher than their own radius, confirming that these sharp asperities are very exposed to contacts and are fast removed.

As the test progresses, sharper asperities disappear so they can no longer contribute to wear, shifting the peak of the histogram towards the next group of sharp asperities. In addition, the surrounding areas become more exposed to contacts and the area of influence of wear becomes wider, as it was observed in Figs. 11 and 12. This results in a progressively wider histogram.

As asperities become large enough, wear becomes a more stable process, which explains the curve of mass loss (Fig. 3 and [8]) and its trend towards a constant mass loss rate by the end of the Micro-Deval test.

5 Conclusions

The Micro-Deval test served as a way to artificially obtain an accelerated ageing of High-Speed Railway ballast grains. The evolution of the morphology of the grains was tracked by scanning a sample of seven grains using X-ray CT at five different states of wear.

A standard Micro-Deval test has proven not to be enough to change the general form of granite grains. Form parameters do not show a clear trend or change all along the test, with the exception of occasional major breakages. Grains

remain recognisable all along the test. On the other hand, SHS analysis showed a significant decrease in angularity and surface texture descriptors. Thus a detailed analysis of the evolution of the asperity radius was performed.

Convex asperities, especially sharper areas (i.e. higher curvature or smaller asperity radius), are generally the most exposed to eventual contacts and impacts with other ballast grains or with the metallic cylinder. In addition, due to their smaller cross-section, these sharp asperities show a weaker resistance to contacts. Thus they tend to disappear on the first minutes of the test, either by getting progressively rounded or by small breakages. As the asperities become rounder, contact area and cross section increases, improving the resistance to wear. Wear may then expose other asperities to contacts, so far protected by sharper features. This leads to an evolution of edges from narrow sharp weak lines to wider and stronger bands, reducing the wear rate of the grain.

Angularity is a desired feature in ballast grains that helps to increase the shear resistance of the layer. However, it represents its main weakness against wear and, therefore, an important source of fine particles to the track.

Acknowledgements This work has been supported by the Lines, Track and Environment Department in Engineering and Projects of SNCF-Réseau and by the Laboratoire 3SR. Laboratoire 3SR is part of the LabEx Tec 21 (Investissements d'Avenir Grant Agreement Number ANR-11-LABX-0030).

Compliance with ethical standards

Conflict of interest The authors declare that they have no conflict of interest.

References

- Ando, E.: Experimental investigation of microstructural changes in deforming granular media using X-ray tomography. Theses, Université de Grenoble (2013). <https://tel.archives-ouvertes.fr/tel-01144326>
- Azéma, E.: Numerical study of granular material composed by polyedric grains : quasi-static rheology, vibrationnal dynamic and application to tamping process. Theses, Université Montpellier II—Sciences et Techniques du Languedoc (2007). <https://tel.archives-ouvertes.fr/tel-00184757>
- Azéma, E., Radjai, F., Dubois, F.: Packings of irregular polyhedral particles: strength, structure, and effects of angularity. *Phys. Rev. E Stat. Nonlinear Soft Matter Phys.* **87**(062203), 1–15 (2013). <https://doi.org/10.1103/PhysRevE.87.062203>
- Azéma, E., Radjai, F., Saussine, G.: Quasistatic rheology, force transmission and fabric properties of a packing of irregular polyhedral particles. *Mech. Mater.* **41**(6), 729–741 (2009). <https://doi.org/10.1016/j.mechmat.2009.01.021>. (Advances in the dynamics of granular materials)
- Barksdale, R.D., Kemp, M.A., Sheffield, W.J., Hubbard, J.L.: Measurement of aggregate shape, surface area, and roughness. *Transportation Research Record* (1301) (1991)

6. Bentley, J.L.: Multidimensional binary search trees used for associative searching. *Commun. ACM* **18**(9), 509–517 (1975). <https://doi.org/10.1145/361002.361007>
7. Besl, P.J., McKay, N.D.: A method for registration of 3-d shapes. *IEEE Trans. Pattern Anal. Mach. Intell.* **14**(2), 239–256 (1992). <https://doi.org/10.1109/34.121791>
8. Quintanilla, I.D., Combe, G., Emeriault, F., Toni, J.-B., Voivret, C., Ferrellec, J.F.: Wear of sharp aggregates in a rotating drum. *EPJ Web Conf.* **140** 07009, (2017). <https://doi.org/10.1051/epjconf/201714007009>
9. Domokos, G., Jerolmack, D.J., Sipos, A.Á., Török, Á.: How river rocks round: resolving the shape-size paradox. *PLOS One* **9**(2), 1–7 (2014). <https://doi.org/10.1371/journal.pone.0088657>
10. Ferrellec, J.F., McDowell, G.: A simple method to create complex particle shapes for dem. *Geomech. Geoeng.* **3**(3), 211–216 (2008). <https://doi.org/10.1080/17486020802253992>
11. Garboczi, E.J.: Three-dimensional mathematical analysis of particle shape using X-ray tomography and spherical harmonics: application to aggregates used in concrete. *Cem. Concr. Res.* **32**, 1621–1638 (2002)
12. Garland, M., Heckbert, P.S.: Surface simplification using quadric error metrics. In: *Proceedings of the 24th Annual Conference on Computer Graphics and Interactive Techniques, SIGGRAPH '97*, pp. 209–216. ACM Press/Addison-Wesley Publishing Co., New York, NY, USA (1997). <https://doi.org/10.1145/258734.258849>
13. Goldman, R.: Curvature formulas for implicit curves and surfaces. *Comput. Aided Geom. Des.* **22**(7), 632–658 (2005). <https://doi.org/10.1016/j.cagd.2005.06.005>. (Geometric Modelling and Differential Geometry)
14. Guennebaud, G., Gross, M.: Algebraic point set surfaces. *ACM Trans. Gr.* **26**(3), 23–9 (2007)
15. Hoppe, H.: New quadric metric for simplifying meshes with appearance attributes. In: *Proceedings of the 10th IEEE Visualization 1999 Conference (VIS '99), VISUALIZATION '99*. IEEE Computer Society, Washington, DC, USA (1999). <http://dl.acm.org/citation.cfm?id=832273.834119>
16. Hsieh, J.: *Computed Tomography: Principles, Design, Artifacts, and Recent Advances*, 2nd edn., vol. PM188. SPIE Press Monograph (2009). <https://doi.org/10.1117/3.817303>
17. Huttenlocher, D.P., Klanderman, G.A., Rucklidge, W.J.: Comparing images using the hausdorff distance. *IEEE Trans. Pattern Anal. Mach. Intell.* **15**(9), 850–863 (1993). <https://doi.org/10.1109/34.232073>
18. Indraratna, B., Ngo, N.T., Rujikiatkamjorn, C., Vinod, J.S.: Behavior of fresh and fouled railway ballast subjected to direct shear testing: discrete element simulation. *Int. J. Geomech.* **14**(1), 34–44 (2014). [https://doi.org/10.1061/\(ASCE\)GM.1943-5622.0000264](https://doi.org/10.1061/(ASCE)GM.1943-5622.0000264)
19. Irazábal González, J.: Numerical analysis of railway ballast behaviour using discrete element method. Ph.D. thesis, Universitat Politècnica de Catalunya (2017). <https://www.tesisenred.net/handle/10803/461536>
20. Kim, H., Haas, C., Rauch, A., Browne, C.: Wavelet-based three-dimensional descriptors of aggregate particles. *J. Transp. Res. Rec.* **1787**, 109–116 (2002)
21. Kline, M.: *Calculus: an intuitive and physical approach*. Dover books on mathematics. Dover, New York (1998)
22. Krumbein, W.C.: Measurement and geological significance of shape and roundness of sedimentary particles. *J. Sediment. Res.* **11**(2), 64 (1941). <https://doi.org/10.1306/D42690F3-2B26-11D7-8648000102C1865D>
23. Kutay, M.E., Ozturk, H.I., Abbas, A.R., Hu, C.: Comparison of 2d and 3d image-based aggregate morphological indices. *Int. J. Pavement Eng.* **12**(4), 421–431 (2011). <https://doi.org/10.1080/10298436.2011.575137>
24. Lecocq, C.: La dégradation du ballast. Memoire. Chaire de Constructions Civiles. Conservatoire National des Arts et Metiers (1985)
25. Lim, W.L.: Mechanics of railway ballast behaviour. Ph.D. thesis, University of Nottingham (2004). <http://eprints.nottingham.ac.uk/10060/>
26. Lu, M.: Discrete element modelling of railway ballast. Ph.D. thesis, University of Nottingham (2008). <http://eprints.nottingham.ac.uk/10611/>
27. Lu, M., McDowell, G.R.: The importance of modelling ballast particle shape in the discrete element method. *Granul. Matter* **9**(1), 69 (2006). <https://doi.org/10.1007/s10035-006-0021-3>
28. Masad, E., Saadeh, S., Al-Rousan, T., Garboczi, E., Little, D.: Computations of particle surface characteristics using optical and X-ray CT images. *Comput. Mater. Sci.* **34**(4), 406–424 (2005). <https://doi.org/10.1016/j.commatsci.2005.01.010>
29. McDowell, G.R., Li, H.: Discrete element modelling of scaled railway ballast under triaxial conditions. *Granul. Matter* **18**(3), 66 (2016). <https://doi.org/10.1007/s10035-016-0663-8>
30. McDowell, G.R., Lim, W.L., Collop, A.C., Armitage, R., Thom, N.H.: Comparison of ballast index tests for railway trackbeds. In: *Proceedings of the Institution of Civil Engineers—Geotechnical Engineering*, vol. 157(3), pp. 151–161 (2004). <https://doi.org/10.1680/jeng.2004.157.3.151>
31. Mitchell, J., Soga, K.: *Fundamentals of soil behavior*. Wiley, New York (2005). https://books.google.fr/books?id=b_dRAAAAMAAJ
32. NF EN 1097-1: Tests for mechanical and physical properties of aggregates—part 1. Determination of the resistance to wear (micro-deval). Standard, AFNOR (2011)
33. NF EN 13450: Aggregates for railway ballast. Standard, AFNOR (2003)
34. Ouhbi, N., Voivret, C., Perrin, G., Roux, J.N.: 3d particle shape modelling and optimization through proper orthogonal decomposition. *Granul. Matter* **19**(4), 86 (2017). <https://doi.org/10.1007/s10035-017-0771-0>
35. Quezada, J.C.: Mechanisms of ballast settlement and its variability. Theses, Université Montpellier II—Sciences et Techniques du Languedoc (2012). <https://tel.archives-ouvertes.fr/tel-01067945>
36. Saint-Cyr, B., Szarf, K., Voivret, C., Azéma, E., Richefeu, V., Delenne, J.Y., Combe, G., Nouguier-Lehon, C., Villard, P., Sorinay, P., Chaze, M., Radjai, F.: Particle shape dependence in 2d granular media. *Europhys. Lett. (EPL)* **98**(4), 44008 (2012)
37. Saussine, G.: Contribution for the modelling of three-dimensional granular matter : study of railway ballast. Theses, Université Montpellier II—Sciences et Techniques du Languedoc (2004). <https://tel.archives-ouvertes.fr/tel-00077519>
38. Selig, E.T., Waters, J.M.: *Track Geotechnology and Substructure Management*. Thomas Telford Publishing (1994). <https://doi.org/10.1680/tgasm.20139>
39. Voivret, C., Nhu, V.H., Perales, R.: Discrete element method simulation as a key tool towards performance design of ballasted tracks. *Int. J. Railw. Technol.* **5**, 83–98 (2016)
40. Voivret, C., Perales, R., Saussine, G.: Ballasted track maintenance with a multi-unit tamping machine: A numerical discrete efficiency comparison. In: *Proceedings of the Second International Conference on Railway Technology: Research, Development and Maintenance*, 53. Civil-Comp Press (2014)
41. Wang, L., Park, J.Y., Fu, Y.: Representation of real particles for dem simulation using X-ray tomography. *Constr. Build. Mater.* **21**(2), 338–346 (2007). <https://doi.org/10.1016/j.conbuildmat.2005.08.013>

42. Wang, L.B., Frost, J.D., Lai, J.S.: Three-dimensional digital representation of granular material microstructure from X-ray tomography imaging. *J. Comput. Civil Eng.* **18**(1), 28–35 (2004)
43. Zingg, T.: Beitrag zur schotteranalyse. Ph.D. thesis, ETH Zurich (1935). <https://doi.org/10.3929/ethz-a-000103455>. SA aus: Schweizerische mineralogische und petrographische Mitteilungen, Band 15, 1935, S.39-140. Diss. Naturwiss. ETH Zürich, Nr. 849, 1935 (Ref.: Niggli, P. ; Korref.: Burri, C)